Supplementary Materials

High-resolution view of the type III secretion export apparatus *in situ* reveals membrane remodeling

Carmen Butan, Maria Lara-Tejero, Wenwei Li, Jun Liu, and Jorge E. Galán

This PDF file includes
Materials and Methods
13 Supplementary Figures
4 Supplementary Tables

www.pnas.org/cgi/doi/10.1073/pns.1916331116

Materials and Methods

Bacterial strains and plasmids

All bacterial strains used in this study are derived from *Salmonella enterica* serovar Typhimurium strain SL1344 (1) and are listed in SI Appendix, Table S2. All strains were constructed by allelic exchange (2) and all plasmids were constructed by Gibson assembly (3).

Analysis of type III protein secretion function

The functionality of the SPI-1 T3SS in the *S*. Typhimurium strains was assessed by examining their ability to secrete type III secreted proteins to the culture supernatant as previously described (4).

Isolation of needle complexes substructures

The needle complex purification from the different *S*. Typhimurium strains was carried out as follows. An MBP-tagged PrgH allele, and when indicated a Δ*invG* allele (to remove the outer rings and neck of the needle complex) were introduced into the different *S*. Typhimurium strains as indicated above. Two liters of 0.3M NaCl containing 100 µg/ml of ampicillin and 0.1% arabinose were inoculated with the different strains and grown for ~10 hs under gentle (100 rpm) shaking. Cells were recovered by centrifugation at 6,000 rpm for 20 minutes, resuspended in 10 ml of lysis buffer [200mM Tris pH 7.5, 20% sucrose, 1mM EDTA, 0.25mg/ml of lysozyme and cOmplete™ EDTA-free protease inhibitor cocktail (Sigma 4693159001)] and incubated on ice for 1 hr. Cells were subsequently incubated for 5 min at 37ºC and lysed by the addition of 0.5% N-Dodecyl-ß-D-maltoside (DDM) (Anatrace D310S). Cells were incubated at 37ºC for additional 5 to 10 min while monitoring lysis, transferred to ice, and further incubated for 1 hr. Debris was removed by centrifugation at 14,000 rpm for 1 hour and the clarified lysate was transferred to a fresh tube. Two hundred microliters of amylose resin (NEB E8021) were added and the suspension was incubated O/N at 4ºC under rocking conditions. Beads were then washed 4x with 10 ml of washing buffer (20 mM Tris pH 7.5, 100 mM NaCl, 1 mM EDTA) and finally resuspended in 50 µl of washing buffer containing 20 mM of maltose. After 1 hr incubation on ice with occasional tapping, beads were removed by centrifugation (3,000 rpm for 5 min) and the needle complex containing supernatant was transferred to a fresh tube for further analysis.

Single-particle cryo-electron microscopy

Vitrified specimens were prepared by adding a 3.5 µl drop of the different samples to holey grids (TedPella, Quantifoil grids, Copper, 300 mesh, R1.2/1.3), which had been overlaid with an additional thin layer of carbon. Grids were blotted for 4-5 seconds, then flash-frozen in liquid ethane using a Vitrobot MarkIII or MarkIV instrument, with the chamber maintained at 6-7^{0}C and 100% humidity. Grids were then imaged under two different conditions: (1) Grids overlaid with samples containing the inner membrane rings and the export apparatus were imaged at the National Institute of Health (NIH) on a Titan Krios microscope (Thermo Fisher Scientific) operated at 300-kV cryo-electron microscope equipped with an energy filter (Gatan GIF Quantum), and a post-GIF Gatan K2 Summit direct electron detector. Projection images were obtained with a K2 camera operated in super-resolution counting mode with a physical pixel size of 1.32 Å, and a super-resolution pixel size of 0.66 Å with the nominal defocus range set between -1.25 and -3.25 µm. During the image acquisition, the Gatan K2 Summit direct electron detector was operated in zero-energy-loss mode with a slit width of 20 eV. The dose rate was 4 $e^-/Å^2/s$ at the specimen plane. The total exposure time was 12 s with intermediate

frames recorded every 0.3 s, giving a total of 40 frames per image. The total accumulated dose was ~48 $e^-/Å^2$; (2) Grids overlaid with samples containing the inner membrane rings without the export apparatus were imaged at the Yale West Campus on a Titan Krios microscope (Thermo Fisher Scientific) operated at 300-kV. Projection images were obtained using a Falcon III detector operated in counting mode with a physical pixel size of 1.07 Å and a nominal defocus range between -1.5 and -3.5 µm. The dose rate was 8.47 $e^-/Å^2/s$ at the specimen plane. The total exposure time was 6 s with intermediate frames recorded every 0.2 s, giving a total of 30 frames per image. The total accumulated dose was ~51 $e^-/Å^2$.

Single-particle cryo EM-image Processing

The frames from each exposure were aligned to compensate for drift and beam-induced motion and summed to a single micrograph using MotionCor2 (5) in Relion 2.1 (6, 7). Single particles were manually picked using Relion 2.1, and defocus and astigmatism were estimated with CTFFIND4 (8) using movie frames without dose weighting. For the sample containing the inner membrane rings and the export apparatus, 104,021 particles were extracted from 2x2 down sampled, 1,847 motion corrected and dose-weighted micrographs. The extracted box size was 280x280 pixels. The particles were subjected to rounds of reference-free 2D classification in Relion 2.1 with poorly defined classes discarded at each 2D classification stage. Particles selected after the 2D classification (51,833 particles) were further classified in 3D into 6 classes using as a reference a density map calculated from the known structure of the IR1 (accession code 5TCP), which was low pass-filtered to a resolution of 60 Å. At the end of the 3D classification step, a subset of 25,129 double-layered particles was retained for 3D auto-refinement in Relion 2.1. This resulted in a 3D reconstruction map of the double-layered particles with a reported overall resolution of 3.9 Å estimated based on the Fourier shell correlation (FSC) using the 0.143 cut-off criterion. From the 25,129 double-layered particles set, the signal corresponding to IR1 only was subtracted. The IR1 signal subtraction was followed by a new 2D classification round to further screen the resulting 25,129 particle stack representing IR1 images only. At the end of this 2D classification procedure, a subset of 23,433 particles representing IR1 images only was selected and subjected to 3D auto-refinement with a soft mask, resulting in a 3D reconstruction map with a resolution of 3.3 Å as assessed by the FSC. Local resolution variations were estimated from two half data maps using ResMap (9). For the sample of inner membrane rings without the export apparatus, 43,040 particles were extracted from 1,567 motion corrected and dose-weighed micrographs. The extracted box size was 360x360 pixels. The extracted particles were subjected to several rounds of 2D classification in Relion 2.1 with poorly defined classes discarded at each 2D classification stage. After the 2D classification 27,433 particles were selected and further classified in 3D into 6 classes. At the end of the 3D classification procedure, a set of 13,732 particles representing the most homogeneous subset of 23-membered rings was retained for refinement in Relion 2.1. The resolution of the final map was estimated to be 5.2 Å as assessed by the FSC. This set of particles was subsequently subjected to a new 2D classification round to select for good quality IR1 images. A subset of 10,674 particles representing IR1 only was 3D reconstructed imposing 23-fold symmetry. This improved the resolution of the IR1 to 3.53 Å as assessed by the FSC. Local resolution estimations were calculated from two half data maps using ResMap (9).

Single particle cryo EM model fitting, refinement and validation

The cryo-EM structure of the IR1 (PDB code: 6DUZ) was fitted by using rigid body fitting into the local resolution filtered 3.3 Å IR1 map, using UCSF Chimera (10). This was

followed by multiple rounds of structure refinement using PHENIX real- space refinement (11) to improve the model geometry and fit to the 3.3 Å IR1 map. Geometric and secondary-structure element restraints were maintained throughout the refinement to minimize over-fitting. The outliers were corrected in Coot (12). A model for the 23-membered ring was constructed in UCSF Chimera (10) using a monomer subunit from the PDB entry 6DUZ which was sequentially fitted and rigid body refined into the 23-subunits of the local resolution filtered 3.53 Å IR1 map. The resulting 23-membered ring model was further optimized using PHENIX real-space refinement (11) with geometric and secondary-structure element restraints maintained throughout the refinement to minimize over-fitting. The outliers were corrected in Coot (12). Overall model quality and geometry outliers for final models were reported using MolProbity (13). Details about the maps and final models are presented in Table S3.

Electron microscopy and negative staining

Four-microliter drops of a sample containing needle complex preparations were applied to glow-discharged, carbon-coated copper grids and after 30 seconds, samples were blotted with filter paper. Subsequently, 4 µl of a 2% (wt/vol) solution of uranyl acetate was added to the grids for 1 minute and the excess stain was removed by blotting with filter paper. Images of negative-stained samples were recorded with a Gatan 4k-by-4k CCD camera on an FEI Technai T12 (120KV) microscope. A total of 71 micrographs with 7,279 selected particles were imaged for samples containing needle complexes from wild type S. Typhimurium, 52 micrographs with 4,346 selected particles for the PrgK$^{\Delta 94\text{-}95}$ mutant, 91 micrographs with 4,943 selected particles for the PrgK$^{\Delta 93\text{-}95}$ mutant, and 192 micrographs with a total of 2,936 selected particles for the PrgK$^{\Delta 93\text{-}96}$ mutant. Particle picking and several cycles of classification and averaging were performed with Relion 2.1 (6, 7).

Cryo-ET sample preparation

Cryo-ET samples obtained from wild type S. Typhimurium and several export apparatus mutants (SI Appendix, Table S4) were prepared as previously described (14). Briefly, minicell producing bacterial strains were grown overnight at 37 °C in LB containing 0.3M NaCl. Fresh cultures were prepared from a 1:100 dilution of the overnight culture and then grown at 37 °C to late log phase in the presence of ampicillin (200 µg/mL) and L-arabinose (0.1%) to induce the expression of regulatory protein HilA and thus increase the number of injectisomes partitioning to the minicells. To enrich for minicells, the culture was centrifuged at 1,000 ×g for 5 min to remove normal-size bacterial cells, and the supernatant fraction was further centrifuged at 20,000 ×g for 20 min to collect the minicells. The minicell pellet was resuspended in PBS and mixed with 10 nm colloidal gold particles and deposited onto freshly glow-discharged, holey carbon grids for 1 min. The grids were blotted with filter paper and rapidly frozen in liquid ethane, using a gravity-driven plunger apparatus as previously described (14).

Cryo-ET data collection and reconstruction

The frozen-hydrated specimens were imaged with a 300kV electron microscope (Titan Krios, Thermo Fisher Scientific) equipped with an energy filter (Gatan) with VPP; the effective pixel size was 2.7 Å. Images were collected automatically using SerialEM (15) in dose fraction mode. The cumulative electron dose for each single-axis tilt series was ~50e/Å^2, distributed over 35 images and covering an angular range of -51° to +51° with increments of 3°. Raw images were processed using MotionCor2 (5). The tilt series were aligned automatically using IMOD (16). Tomograms were generated by using TOMO3D

(17). In total, 1,266 tomograms (3,839 × 3,710 x 1,800 voxels) were generated for detailed examination of the export apparatus in several mutants (SI Appendix, Table S4).

Subtomogram analysis

Subtomogram analysis was accomplished as described previously to analyze the injectisomes (14). Briefly, we first visually identified the injectisomes on each minicell. Two coordinates along the needle were used to estimate the initial orientation of each particle assembly. For initial analysis, 4 × 4 × 4 binned subtomograms (100 × 100 × 100 voxels) of the intact injectisome were used for alignment and averaging by using the tomographic package I3 (18, 19). Then multivariate statistical analysis and hierarchical ascendant classification were used to analyze the injectisome (20). Importantly, no symmetry was applied at the beginning of the alignment to resolve the symmetry mismatch as shown in Fig. 6D. To better visualizing the InvA ring in detail, 9-fold symmetry was applied to unbinined subtomograms (400 × 400 × 400 voxels).

Three-Dimensional Visualization and Modeling

IMOD (16) was used to take snapshots of 2D slices from 3D tomograms and UCSF Chimera (10) was used for surface rendering of 3D averaged structures. The pseudo atomic model was built by docking the atomic structures of an InvA homolog (PDB-4A5P)(21), SpaP/SpaQ/SpaR homologs (PDB-6F2E), (22), InvC/InvI homologs (PDB-6NJP) (23), and the needle complex (PDB-5TCR) (24). Animations were generated using UCSF ChimeraX and edited with iMovie.

References

1. Hoiseth SK & Stocker BA (1981) Aromatic-dependent *Salmonella typhimurium* are non-virulent and effective as live vaccines. *Nature* 291:238-239.
2. Kaniga K, Bossio JC, & Galan JE (1994) The Salmonella typhimurium invasion genes invF and invG encode homologues of the AraC and PulD family of proteins. *Mol Microbiol* 13(4):555-568.
3. Gibson D*, et al.* (2009) Enzymatic assembly of DNA molecules up to several hundred kilobases. *Nature Methods* 6 343–345.
4. Lara-Tejero M*, et al.* (2019) Role of SpaO in the assembly of the sorting platform of a Salmonella type III secretion system. *PLoS Pathog.* 15:e1007565.
5. Zheng S*, et al.* (2017) MotionCor2: anisotropic correction of beam-induced motion for improved cryo-electron microscopy. *Nature Methods* 14: 331-332.
6. Scheres SH (2012) A Bayesian view on cryo-EM structure determination. . *J Mol. Biol.* 415:406-418.
7. Scheres SH (2012) RELION: implementation of a Bayesian approach to cryo-EM structure determination. *J. Struct. Biol.* 180: 519-530.
8. Rohou A & Grigorieff N (2015) CTFFIND4: Fast and accurate defocus estimation from electron micrographs. *J. Struct. Biol.* 192:216-221.
9. Kucukelbir A, Sigworth F, & Tagare H (2014) Quantifying the local resolution of cryo-EM density maps. *Nat Methods.* 11:63-65

10. Pettersen EF, *et al.* (2004) UCSF Chimera--a visualization system for exploratory research and analysis. *J. Comput. Chem.* 25:1605-1612.
11. Adams P, *et al.* (2010) PHENIX: a comprehensive Python-based system for macromolecular structure solution. *Acta Cryst.* D66:213-221.
12. Emsley P & Cowtan K (2004) Coot: model-building tools for molecular graphics. *Acta Crystallogr.* D 60:2126–2132.
13. Williams CJ, *et al.* (2018) MolProbity: More and better reference data for improved all-atom structure validation. *Protein Sci* 27:293-315.
14. Hu B, Lara-Tejero M, Kong Q, Galán J, & Liu J (2017) In Situ Molecular Architecture of the Salmonella Type III Secretion Machine. *Cell* 168:1065-1074. .
15. Mastronarde D (2005) Automated electron microscope tomography using robust prediction of specimen movements. *J Struct Biol.* 152:36-51.
16. Mastronarde D & Held S (2017) Automated tilt series alignment and tomographic reconstruction in IMOD. *J Struct. Biol.* 197:102-113.
17. Agulleiro JI & Fernandez JJ (2015) Tomo3D 2.0--exploitation of advanced vector extensions (AVX) for 3D reconstruction. *J. Struct. Biol.* 189:147-152.
18. Winkler H & Taylor KA (2006) Accurate marker-free alignment with simultaneous geometry determination and reconstruction of tilt series in electron tomography. *Ultramicroscopy* 106(3):240-254.
19. Winkler H, *et al.* (2009) Tomographic subvolume alignment and subvolume classification applied to myosin V and SIV envelope spikes. *J Struct Biol* 165(2):64-77.
20. Winkler H, *et al.* (2009) Tomographic subvolume alignment and subvolume classification applied to myosin V and SIV envelope spikes. *J. Struct Biol* 165: 64-77.
21. Abrusci P, *et al.* (2013) Architecture of the major component of the type III secretion system export apparatus. *Nat Struct Mol Biol.* 20:99-104.
22. Kuhlen L, *et al.* (2018) Structure of the core of the type III secretion system export apparatus. *Nat Struct Mol Biol.* 25:583-590.
23. Majewski DD, *et al.* (2019) Cryo-EM structure of the homohexameric T3SS ATPase-central stalk complex reveals rotary ATPase-like asymmetry. . *Nat. Commun.* 10:626-638.
24. Worrall LJ, *et al.* (2016) Near-atomic-resolution cryo-EM analysis of the Salmonella T3S injectisome basal body. *Nature* 540:597-601.

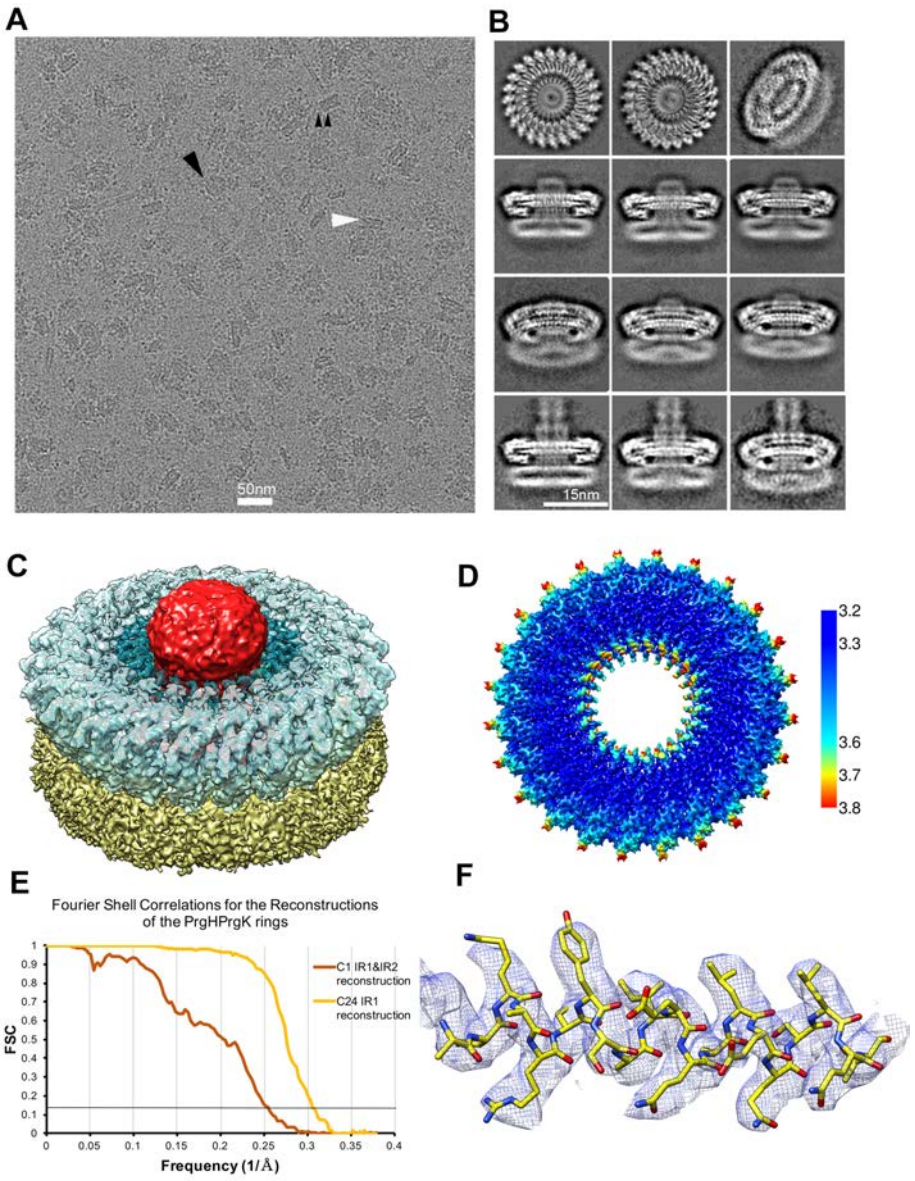

Fig. S1. Cryo-EM structure of the needle complex IR1 and IR2 containing the core components of the export apparatus. **(A)** Representative cryo-EM micrograph. (**B**) Subset of selected 2D class averages. (**C**) 3D structure of IR1 (blue), IR2 (yellow) and the core components of the export apparatus (red). (**D**) Cryo EM structure of the IR1 colored according to the local resolution (in Å). (**E**) Fourier shell correlations (FSC) of the reconstructions of the IR1 and IR2 rings. (**F**) Representative cryo-EM local densities with refined atomic models for residues 100-119 of PrgK.

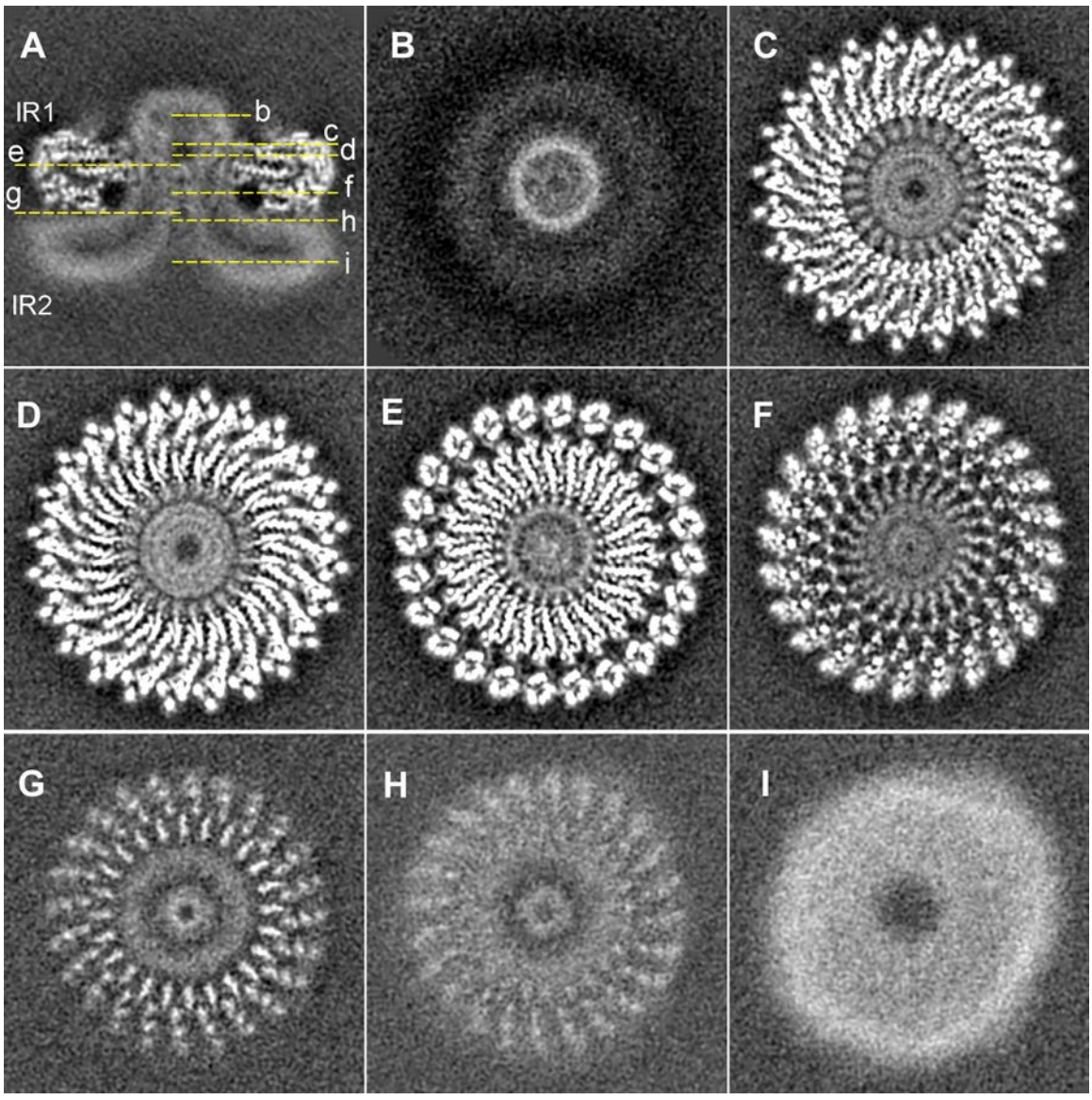

Fig. S2. Horizontal sections through the 3D reconstructions of the needle complex IR1 and IR2 containing the core components of the export apparatus. The position of the sections depicted in panels **B** through **I** are indicated in panel **A**.

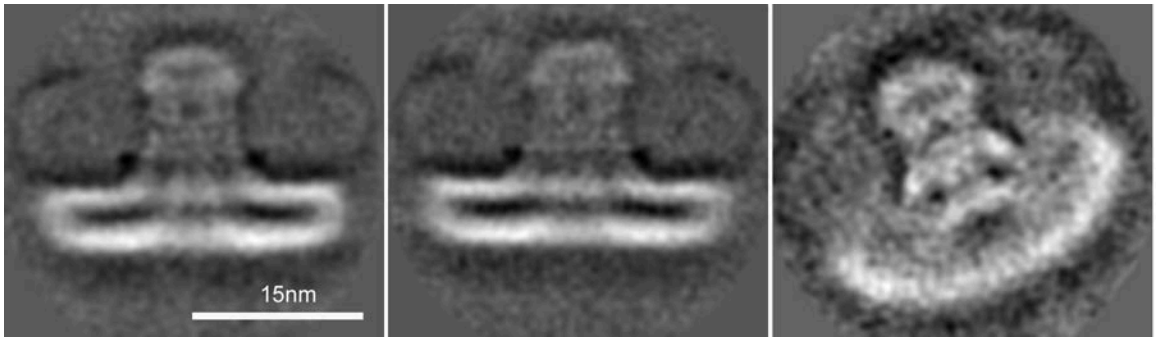

Fig. S3. Densities corresponding to IR2, export apparatus, and associated membranes after subtraction of the densities associated with IR1.

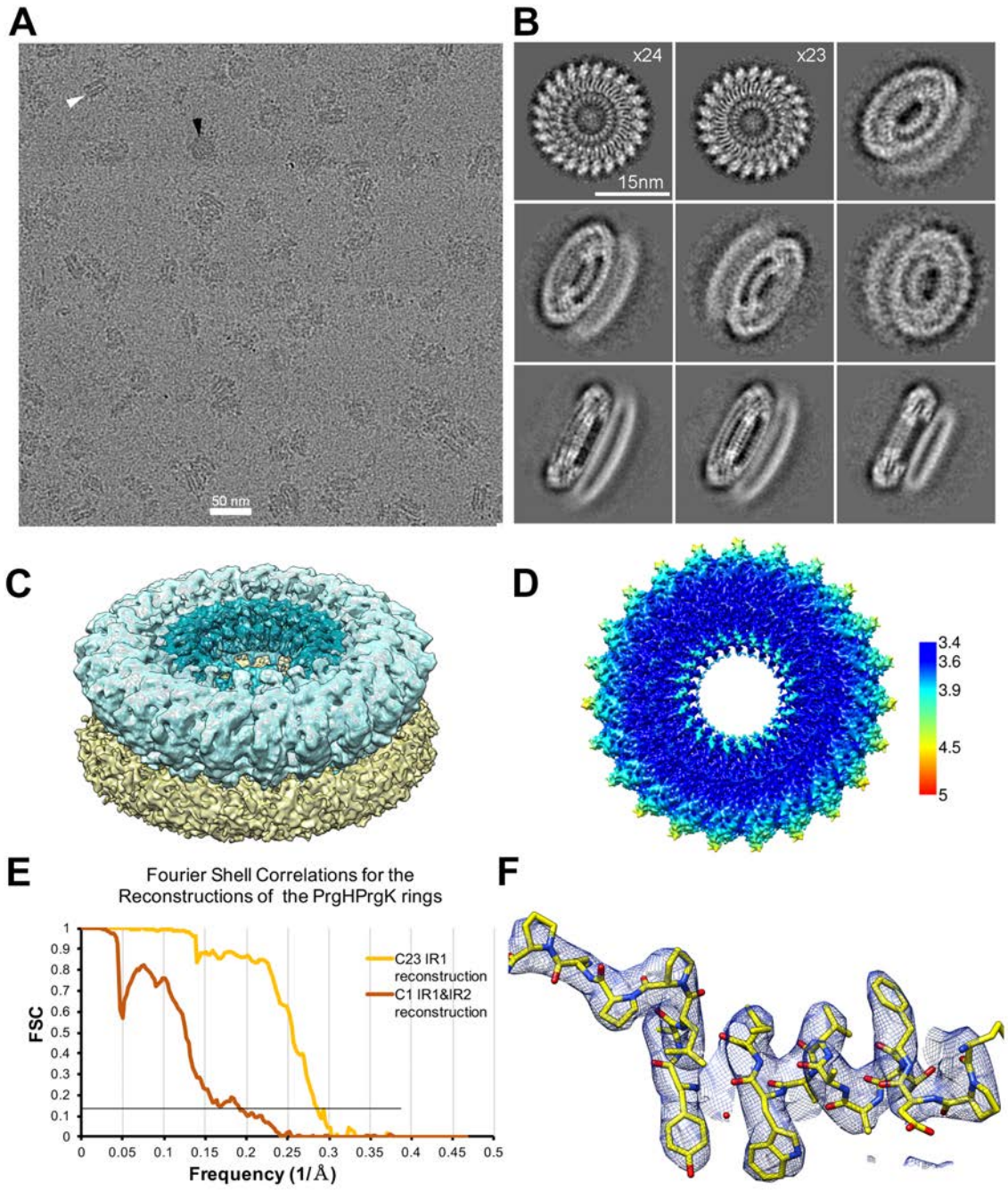

Fig. S4. Cryo-EM structure of the needle complex IR1 and IR2 assembled in the absence of the export apparatus showing 23-fold symmetry **(A)** Representative cryo-EM micrograph. (**B**) Subset of selected 2D class averages. (**C**) 3D structure of IR1 (blue), and IR2 (yellow). (**D**) Cryo EM structure of the IR1 colored according to the local resolution (in Å). (**E**) Fourier shell correlations (FSC) of the reconstructions of the IR1 and IR2 rings. (**F**) Representative cryo-EM local densities with refined atomic models for residues 63-81 of PrgK.

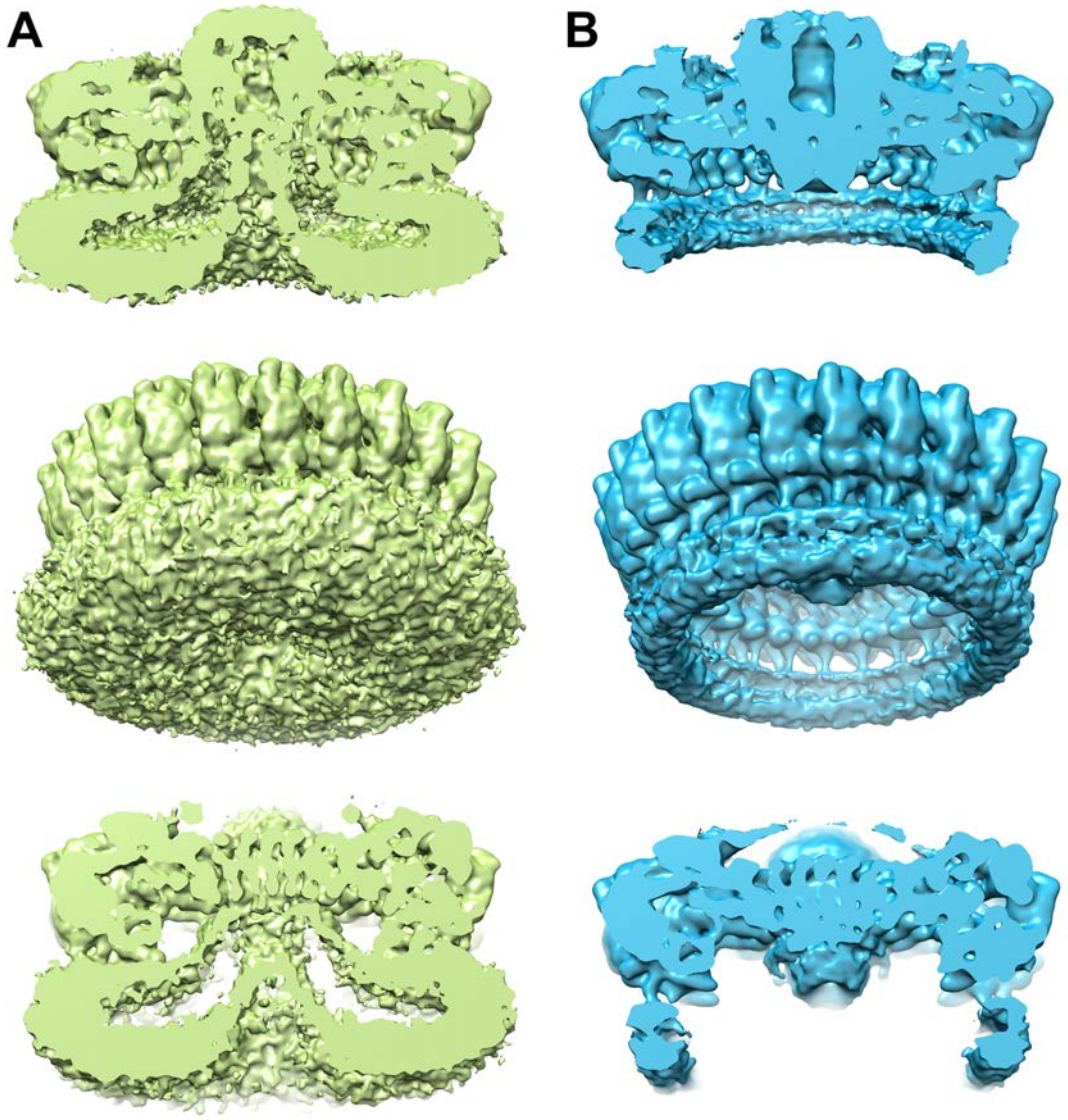

Fig. S5. Comparison of the 3D reconstructions of the structure reported in this study (green) (**A**) with a previously reported structure (accession numbers EMD-8398 and 5TCP) (**B**) isolated under conditions that remove the associated membranes.

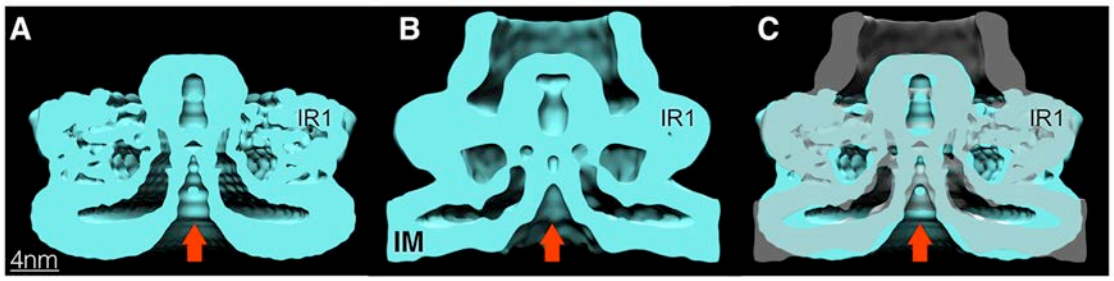

Fig. S6. Comparison of the cryo-EM structure of the isolated needle complex IR1 and IR2 containing the core components of the export apparatus (**A**) with the cryo ET structures of the type III secretion needle complex from a *S*. Typhimurium Δ*invA* mutant strain (**B**). The overlaid structures are shown in (**C**).

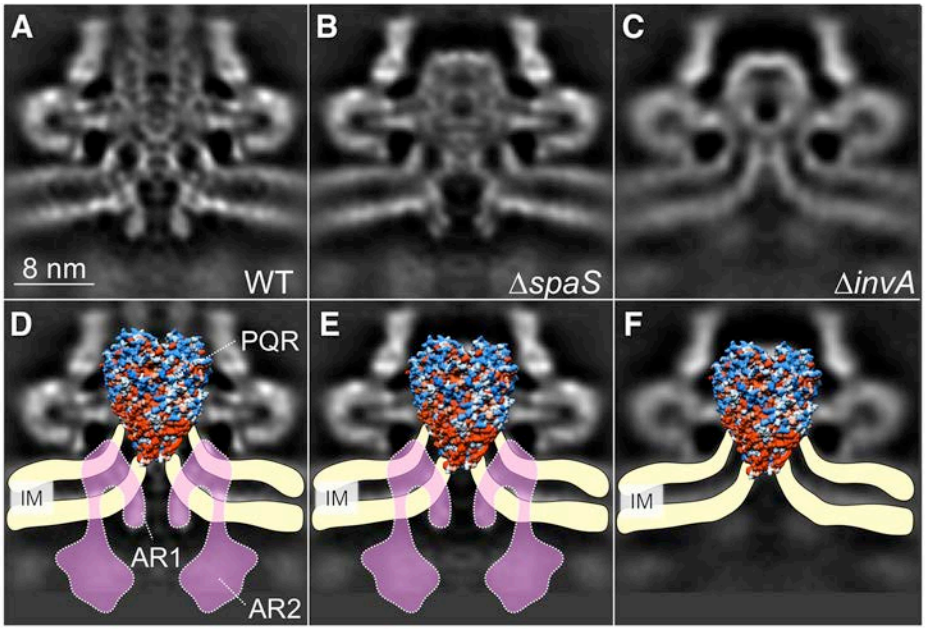

Fig. S7. Vertical sections of the cryo-ET in situ structures of injectisomes obtained from wild-type (WT) (**A** and **D**), ΔspaS (**B** and **E**), and *ΔinvA* (**C** and **F**) *S.* Typhimurium mutant strains. Model of inner membrane (IM) colored in yellow is overlaid on the vertical sections (**D**, **E** and **F**). The model of the architecture of InvA colored in purple is overlaid on the vertical sections from WT (**D**) and the Δ*spaS* mutant(**E**). The location of the InvA AR1 and AR2 is noted.

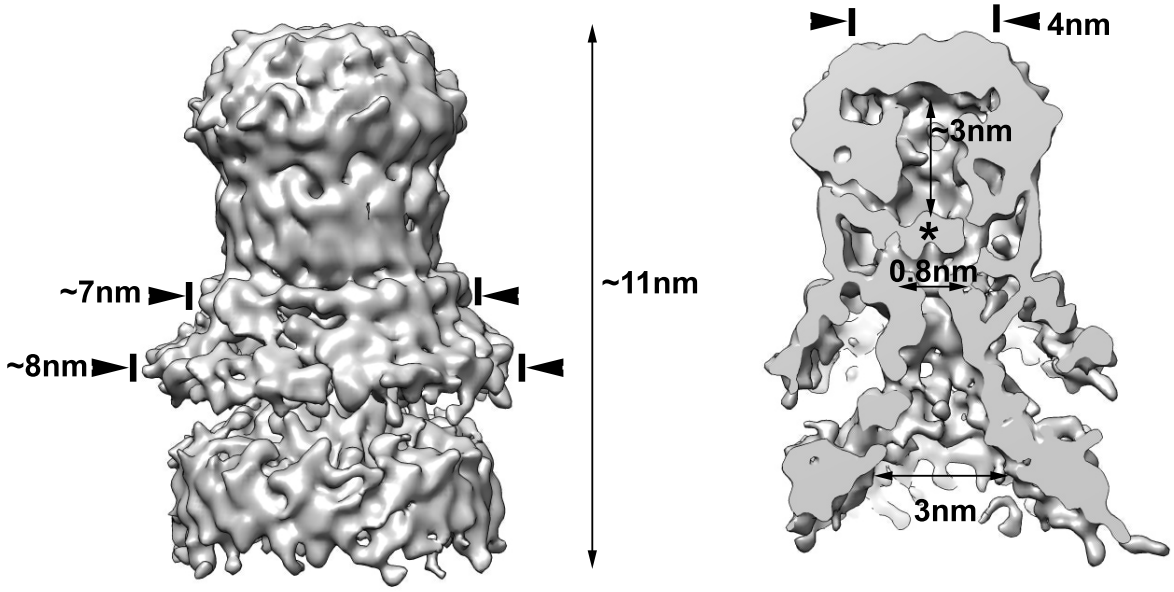

Fig. S8. 3D reconstructions of the core components of the export apparatus and associated membranes after masking the densities corresponding to the IR1 and part of the IR2. In a cut-away view through the 3D reconstruction, an asterix denotes a density that separates the central cavity from the cytoplasmic side of the structure. Relevant dimension are indicated.

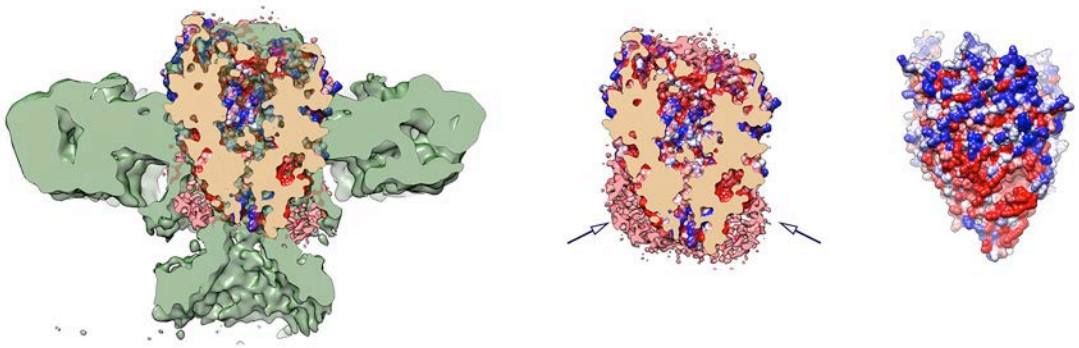

Fig. S9. Overlay of the cryo-EM structure of the needle complex IR1 and IR2 containing the core components of the export apparatus (green) with the structure of the isolated FliP/FliQ/FliR complex (PDB 6F2E). The surface of the FliP/FliQ/FliR complex surface is colored according to hydrophobicity (red -hydrophobic; blue-charged). The location of the detergent belt (in pink, central image) is indicated by arrows.

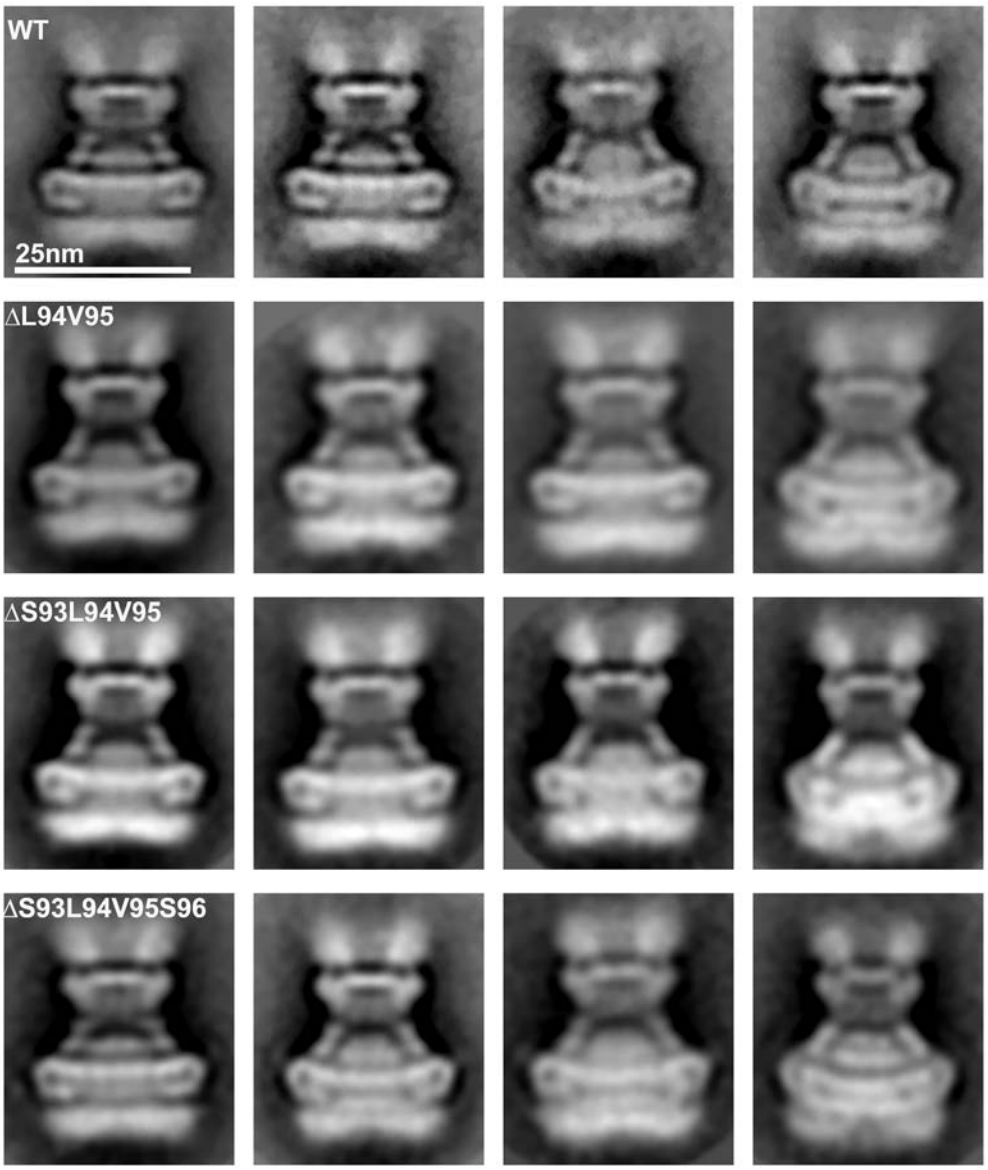

Fig. S10. Mutations in a periplasmic domain of the needle complex protein PrgK that interacts with the core components of the export apparatus do not affect needle complex base structure or export apparatus deployment. Shown are representative class averages of needle complexes isolated from *S*. Typhimurium expressing wild type PrgK or the indicated PrgK deletion mutants.

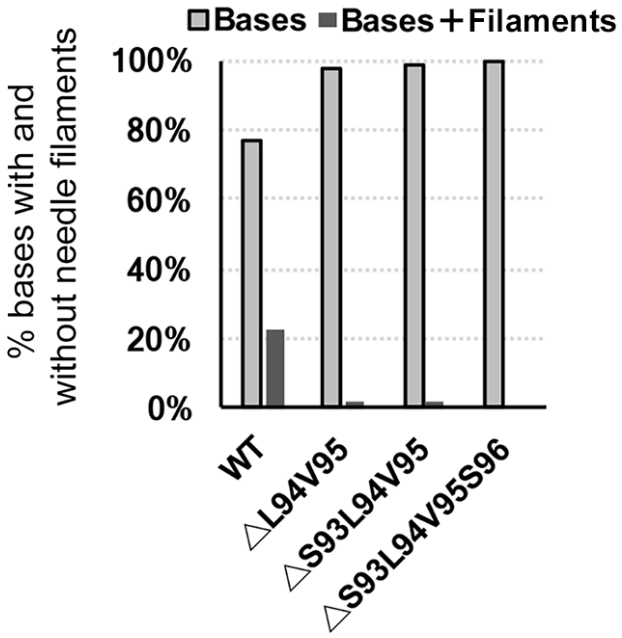

Fig. S11. Deletions mutations in a periplasmic domain of the needle complex protein PrgK impairs needle filament assembly. The graph shows the percentage of needle complex bases with (bases) or without (bases + filaments) needle filaments.

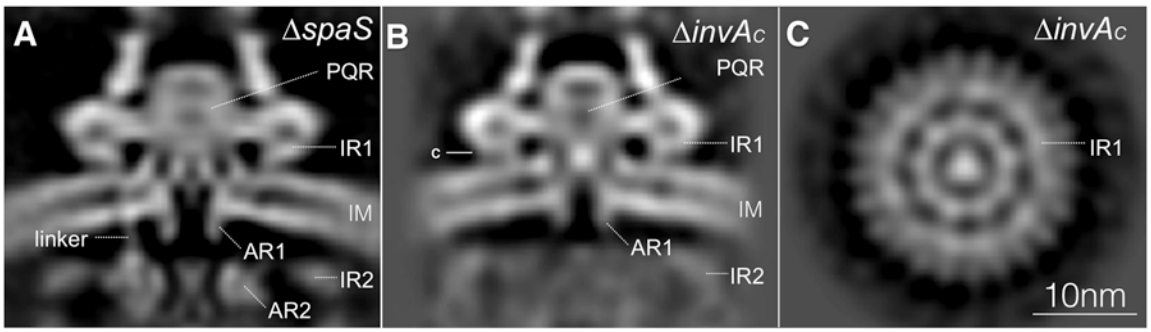

Fig. S12. Vertical sections of the cryo ET *in situ* structures of injectisomes obtained from *S.* Typhimurium Δ*spaS* (**A**), or from a strain expressing a mutant form of InvA that lacks its last 328 amino acids (**B**). Also shown is a horizontal section of the latter structure (**C**). Note the presence of the AR1 ring made by the carboxy-terminal domain of InvA and the absence of AR2 in tomograms from a mutant lacking the last 329 amino acids of InvA, which contains the entire cytoplasmic domain (Δ*invAc*) in panel (**B**). IR1: Inner ring 1; IR2: inner ring 2; AR1: InvA-associated ring 1; AR2: InvA-associated ring 2.IM: inner membrane.

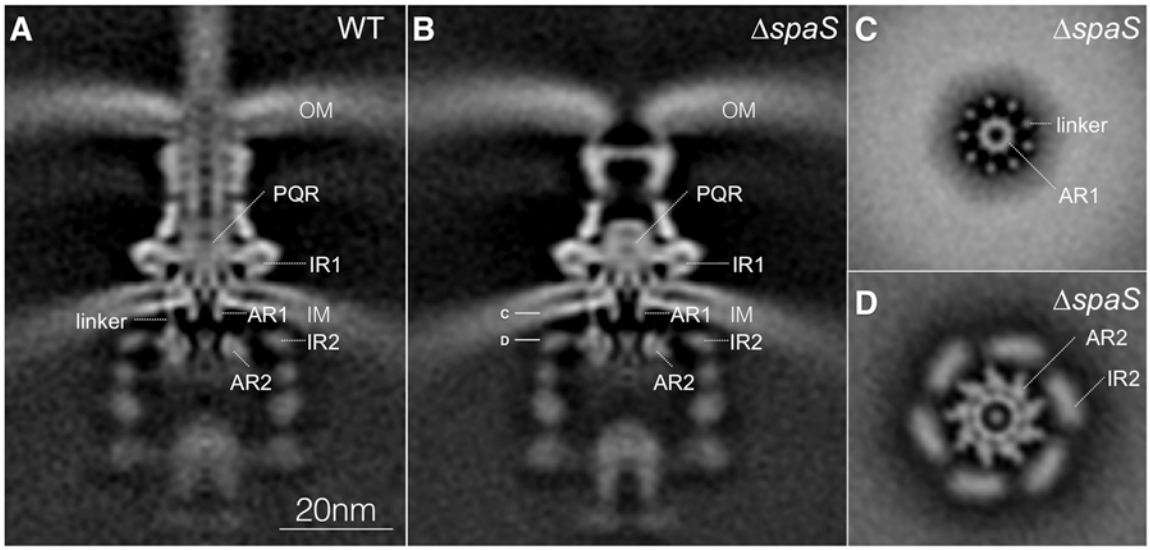

Fig. S13. Vertical sections of the cryo ET *in situ* structures of injectisomes obtained from wild type *S*. Typhimurium (**A**) or Δ*spaS* mutant strain (**B**), Also shown are a horizontal sections of the latter structure strain through the planes indicated in panel B (**C** and **D**). OM: bacterial outer membrane; IM: bacterial inner membrane; IR1 and IR2: inner rings 1 and 2 of the T3SS needle complex; PQR: SpaP/SpaQ/SpaR complex; AR1 and AR2: membrane proximal (AR1) and distal (AR2) cytoplasmic rings of InvA. IR1: Inner ring 1; IR2: inner ring 2; AR1: InvA-associated ring 1; AR2: InvA-associated ring 2.IM: inner membrane.

Table S1: LC-MS/MS analysis of needle complex preparation

Description	Score	Mass	Num. of significant matches	Num. of significant sequences	emPAI
Maltose Binding Protein MalE	34573	42456	860	70	3877
PrgH Needle complex inner membrane protein OS=Salmonella typhimurium (strain SL1344) GN=prgH	16707	44489	485	41	85.44
PrgK Needle complex inner membrane lipoprotein OS=Salmonella typhimurium (strain SL1344) GN=prgK	12411	28250	292	23	53.99
PrgI Type III secretion system apparatus needle protein OS=Salmonella typhimurium (strain SL1344) GN=prgI	2661	8851	81	8	38.16
SpaP Type III secretion system secretory apparatus OS=Salmonella typhimurium (strain SL1344) GN=spaP	1116	25272	51	9	3.44
SpaS Type III secretion system secretory apparatus OS=Salmonella typhimurium (strain SL1344) GN=spaS	982	40410	29	8	1.84
SipD SPI-1 Type III secretion system-tip protein OS=Salmonella typhimurium (strain SL1344) GN=sipD	839	37147	21	13	3.89
PrgJ Needle complex inner rod protein OS=Salmonella typhimurium (strain SL1344) GN=prgJ	639	10920	16	9	42.54
InvA Secretory apparatus of type III secretion system OS=Salmonella typhimurium (strain SL1344) GN=invA	216	76121	9	8	0.56
SpaQ Type III secretion system secretory apparatus OS=Salmonella typhimurium (strain SL1344) GN=spaQ	76	9467	3	2	1.38

Table S2 Strains used in this study

Strain	Genotype	Reference (PMID)
SB3083	*MBP-prgH ΔinvG flhD::Tn10*	This study
SB3098	*MBP-prgH ΔinvG ΔspaPQRS flhD::Tn10*	This study
SB3079	*MBP-prgH flhD::Tn10*	This study
SB3581	*MBP-prgH prgKΔL94V95 flhD::Tn10*	This study
SB3582	*MBP-prgH prgKΔS93L94V95 flhD::Tn10*	This study
SB3583	*MBP-prgH prgKΔS93L94V95S96 flhD::Tn10*	This study
SB1780	*minD::cat*	23481398
SB3112	*ΔinvA minD::cat*	28283062
SB3113	*3xFspaO ΔspaPQRS minD::cat*	28283062
SB3565	*ΔspaS minD::cat*	This study
SB3592	*invAΔ357-685aa-3xF minD::cat*	This study

Table S3. Cryo EM data

Data Collection	#1 PrgH/K ring C1 map	#2PrgH/K ring C24 map	#3PrgH/K ring C1 map	#4PrgH/K ring C23 map
Electron Microscope	Titan Krios	Titan Krios	Titan Krios	Titan Krios
Electron Detector	K2 Summit + GIF (super-resolution mode)	K2 Summit + GIF (super-resolution mode)	Falcon III (EC mode)	Falcon III (EC mode)
Voltage (KV)	300	300	300	300
Pixel size(Å)	0.66	0.66	1.07	1.07
Defocus range (μm)	1.25-3.25	1.25-3.25	1.5-3.5	1.5-3.5
Electron dose (e^-/Å^2)	48	48	51	51
Images	1,847	1,847	1,567	1,567

3D Reconstruction

Symmetry imposed	C1	C24	C1	C23
Initial number of particles	104,021	104,021	43,040	43,040
Final number of particles	25,129	23,433	13,732	10,674
Model resolution range (Å)	3.97	3.3	5.2	3.53
FSC threshold	0.143	0.1433	0.143	0.143
Map sharpening B-factor (Å^2)	-	-134	-	-159

Model composition

Polypeptide chains	24	24	23	23
R.m.s. devaitions				
Bonds(Å)		0.009		0.009
Angles(^{0})		1.048		1.11
Ramachandran plot				
Favored (%)		94.12		93.58
Allowed (%)		5.88		6.42
Outliers (%)		0		0

Validation

Molprobity score		2.12		2
Clash score		4.67		4.45
Rotamer outlier (%)		4.35		3.4

Table S4: Number of tomograms of minicells and sub-tomograms of injectisomes processed in this study

Strain	Relevant Genotype	Tomograms	Sub-tomograms
SB1780	*wild-type*	326	6523
SB3112	Δ*invA*	275	4165
SB3113	Δ*spaPQRS*	241	2368
SB3565	Δ*spaS*	316	5882
SB3592	*invA*Δ	108	992
Total:		1266	19,930

Video captions:

Supplementary Video S1. Docking of the structure of the core components of the export apparatus FliP/FliQ/FliR (surface rendered according to hydrophobicity (red, hydrophobic; blue, charge) onto the cryo EM structure of isolated needle rings of the SPI-1 S. Typhimurium T3SS injectisome containing the export apparatus.

Supplementary Video S2. Localization of the export apparatus component InvA (depicted in pink) relative to the core components of the export apparatus (depicted in yollow) and other structures of the type III secretion injectisome.

Supplementary Video S3. Depiction of the conduit delimited by the InvA cytoplasmic rings that leads to the entrance of the gate of the export apparatus.